JGR Space Physics

RESEARCH ARTICLE
10.1029/2022JA030659

Key Points:

- We model nonlinear feedback interactions between ULF field-aligned currents and the ionospheric plasma
- Simulations show that these interactions produce ULF quarter-waves in the global resonator with a non-symmetric density distribution
- Ionospheric valley enhances this effect by decreasing the effective conductivity of the ionosphere

Correspondence to:
A. V. Streltsov,
streltsa@erau.edu

Citation:
Streltsov, A. V., & Mishin, E. V. (2022). Ionospheric feedback and ULF quarter-waves. *Journal of Geophysical Research: Space Physics*, *127*, e2022JA030659. https://doi.org/10.1029/2022JA030659

Received 16 MAY 2022
Accepted 31 AUG 2022

Author Contributions:
Conceptualization: Evgeny V. Mishin
Formal analysis: Anatoly V. Streltsov
Funding acquisition: Evgeny V. Mishin
Investigation: Anatoly V. Streltsov
Methodology: Evgeny V. Mishin
Software: Anatoly V. Streltsov
Validation: Anatoly V. Streltsov

Ionospheric Feedback and ULF Quarter-Waves

Anatoly V. Streltsov[1] **and Evgeny V. Mishin**[2]

[1]Department of Physical Sciences, Embry-Riddle Aeronautical University, Daytona Beach, FL, USA, [2]Space Vehicles Directorate, Air Force Research Laboratory/RVBXC, Kirtland AFB, Albuquerque, NM, USA

Abstract This paper presents results from the numerical investigation of nonlinear feedback interactions between ULF field-aligned currents (FACs) and the ionospheric plasma in the global magnetospheric resonator with a non-symmetrical distribution of the plasma density in the conjugate hemispheres. The density asymmetry is enhanced by the introduction of the ionospheric valley in the hemisphere where the plasma density is already lower. The main result from this study is that in the non-symmetrical resonator, the ionospheric feedback mechanism, driven by the electric field with the maximum amplitude of 50 mV/m, develops nonlinear, intense, small-scale upward currents with a characteristic quarter-wavelength structure along the ambient magnetic field. The frequency of these waves is two times less than the fundamental frequency of the symmetrical resonator. The ionospheric valleys, which are depletions of the plasma density between the ionospheric *E* and *F* regions, enhance this effect, by reducing the effective ionospheric conductivity. This effect is important for the interpretation of ground, satellite, and sounding rocket observations of ULF waves and FACs in the auroral and subauroral geospace.

1. Introduction

The combination of nonlinear interactions between the magnetospheric field-aligned currents (FACs) and the ionospheric plasma is one of the main mechanisms defining the dynamics, structure, and amplitude of ULF electromagnetic waves and small-scale density structures in the near-Earth space at auroral and subauroral latitudes. The essence of these interactions can be explained as an active ionospheric response to the structure and amplitude of FACs, changing ionospheric conductivity by precipitating and removing electrons from the ionosphere. The change in the conductivity changes the reflection coefficient of the waves and the dissipation of the energy of the large-scale electric field normally existing in the high-latitude ionosphere.

The upward FACs precipitate electrons in the ionosphere and locally increase the ionospheric conductivity. The increase in the conductivity increases the amplitude of the reflected currents and decreases the dissipation of the large-scale electric field in the ionosphere, which, in turn, generates additional upward FACs. Thus, when the geophysical conditions are favorable, the ionosphere provides a positive, constructive feedback on the amplitude of FACs interacting with it. And if this current is trapped in some magnetospheric resonator with at least one boundary on the ionosphere, then the positive feedback may lead to the development of a so-called ionospheric feedback instability (IFI).

The basic concept of IFI has been introduced by Atkinson (1970) and extensively studied after that in the global magnetospheric resonator and the ionospheric Alfvén resonator (IAR) by Sato (1978); Watanabe et al. (1993); Trakhtengertz and Feldstein (1981, 1991); Lysak (1991); Pokhotelov et al. (2000); Pokhotelov et al. (2002a, 2002b); Streltsov and Mishin (2018a). In these studies, the ionosphere is treated as a thin conducting layer (≈10–20 km thick) located near the E-region peak (≈100–110 km altitude) with a uniform density and the electric field over the height of the layer. The ionospheric Hall and Pedersen conductivities are assumed to operate only within this layer. (Although, in the real ionosphere these conductivities maximizes at different altitudes Kelley, 1989). This assumption is justified because the instability typically operates in the frequency range ≤1 Hz (in this paper, we consider the waves with frequencies 6–20 mHz). And the parallel wavelength of these waves is much larger than the characteristic vertical scale-size of the ionosphere. A rigorous analysis justifying treatment of the ionosphere as a thin conducting slab has been carried out by Trakhtengertz and Feldstein (1981, 1991).

These studies show that the main parameters determining the development of the IFI are the large-scale electric field and the plasma density in the ionosphere. The electric field is the energy source for the instability. The density defines the height-integrated Pedersen, Σ_P, and Hall, Σ_H, conductances in the ionosphere

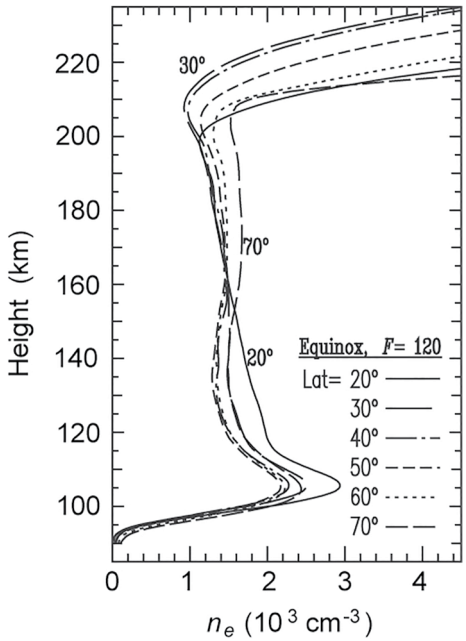

Figure 1. Examples of the ionospheric density valley from Titheridge (2003).

and the so-called wave impedance above the ionosphere, $\Sigma_A = 1/\mu_0 v_A$. Here, $v_A = B_0/\sqrt{\mu_0 \rho}$ is the Alfvén speed, B_0 is the background magnetic field, and ρ is the mass density. Analytical and numerical studies of IFI by Trakhtengertz and Feldstein (1991); Lysak (1991); Pokhotelov et al. (2000); Streltsov and Lotko (2004) show that one of the favorable conditions for the development of the instability is $\Sigma_P \approx \Sigma_A$. This condition postulates the "matching impedance" between the ionosphere and the magnetosphere, which facilitates the energy exchange between these two parts of the coupled magnetosphere-ionosphere system.

Similar conclusions have been derived from the active experiments consisting of the modulating of the ionospheric parameters by heating the ionosphere with ground-based HF transmitters. These experiments demonstrate that the ULF waves with the frequency of the heater modulation were detected in space on the magnetic field lines threading through the heated spot (Robinson et al., 2000). The detailed numerical study by Pokhotelov et al. (2004) explains these observations. More results from the theory, simulations, and experiments related to the generation of ULF waves in the magnetosphere with the artificial ionospheric heating are given in (Streltsov et al., 2018).

In addition, the rapid changes in the ionospheric density between E and F region produce gradients in the background v_A and these gradients may reflect some portion of the ULF waves propagating from the magnetosphere. In that sense, one may say that the parallel gradient in the plasma density changes the effective conductivity of the ionosphere. To make things more complex, the reflection of the ULF waves from such gradients depends on the perpendicular wavenumber (Seyler, 1990): the large-scale part of the ULF wave coming from the magnetosphere can reach the bottom of the ionosphere and smaller-scale part reflects from the density gradient in the ionosphere.

Therefore, one can expect that the structure of the ionospheric plasma density above the E region is an important parameter in the development of the IFI and structure, dynamics, and amplitude of the small-scale FACs, ULF waves, and density irregularities produced by the instability. This paper provides results from numerical simulations of fields and currents produced by IFI when the ionosphere contains a so-called "valley" in the plasma density between E and F regions. The examples of this valley are shown in Figure 1, reproduced from Titheridge (2003).

Our investigation is based on numerical simulations of the reduced two-fluid MHD model describing propagation of dispersive Alfvén waves in the magnetosphere and their interactions with the ionospheric plasma. The model has been used in several papers (e.g., Streltsov & Lotko, 1997; Streltsov & Mishin, 2020), and it is briefly described in the next section for the sake of completeness.

2. Model

Small-scale Alfvén waves in the magnetosphere can be described with the reduced two-fluid MHD model consisting of the electron parallel momentum equation, the density continuity equation, and the current continuity equation (e.g., Chmyrev et al., 1988; Streltsov & Mishin, 2018a):

$$\frac{\partial v_{\parallel e}}{\partial t} + v_{\parallel e}\nabla_\parallel v_{\parallel e} + \frac{e}{m_e}E_\parallel + \frac{1}{m_e n_0}\nabla_\parallel (nT_e) = -\nu_e v_{\parallel e}, \tag{1}$$

$$\frac{\partial n}{\partial t} + \nabla \cdot \left(n v_{\parallel e}\hat{\mathbf{b}}\right) = 0, \tag{2}$$

$$\nabla \cdot j_\parallel \hat{\mathbf{b}} + \frac{1}{\mu_0}\nabla \cdot \left(\frac{1}{c^2} + \frac{1}{v_A^2}\right)\frac{\partial \mathbf{E}_\perp}{\partial t} = 0. \tag{3}$$

The subscripts $\parallel$ and $\perp$ denote vector components in the directions parallel and perpendicular to $\hat{\mathbf{b}} = \boldsymbol{B}_0/B_0$, $v_{\parallel e}$ is the parallel component of the electron velocity, T_e is the background electron temperature, c is the speed of light, and ν_e is the electron collision frequency.

The model includes non-ideal MHD corrections to the parallel electric field associated with the finite electron mass (inertial dispersion) (Goertz & Boswell, 1979) and temperature (kinetic dispersion) (Hasegawa, 1976). These corrections make the model applicable to the waves with relatively small perpendicular sizes (less than 10 km in the ionosphere), which is important for the problem considered in this study, because such small-scale waves carry the most intense FACs interacting with the ionosphere.

Equations 1–3 are solved numerically in a two-dimensional spatial domain representing the part of the magnetosphere bounded by the ionosphere and two dipole magnetic shells, $L = 4.7$ and $L = 5.1$. These shells are chosen to make the modeling results consistent with the observations of the perpendicular electric fields and the ULF waves near the plasmapause reported by Streltsov and Mishin (2018b).

The model has two spatial dimensions: One dimension is along the dipole magnetic field, and another is perpendicular to the dipole magnetic shell. The azimuthal direction is neglected. There are two reasons for such simplification: (a) Many numerical and analytical studies demonstrate that the 2D geometry adequately represents all major features of the ionospheric feedback mechanism, for example, (Lysak, 1991; Pokhotelov et al., 2000); (b) ULF waves and currents produced by the ionospheric feedback mechanism at auroral and subauroral latitudes also frequently demonstrate 2D geometry for example, (Streltsov & Mishin, 2018b, 2020).

Feedback interactions between FACs and the ionosphere are included in the model via the ionospheric boundary conditions connecting the perpendicular electric field $E_\perp$ and the plasma density n_E in the conducting bottom of the ionosphere with the field-aligned current density, $j_\parallel$. Here, the ionosphere is treated as a thin conducting layer with an effective thickness $h \approx 20$ km located at the altitude ≈100–110 km (Miura & Sato, 1980; Sato, 1978). This is a reasonable assumption, because the vertical extend of the conducting portion of the real ionosphere is much less than the parallel wavelength of ULF Alfvén waves.

The ionospheric boundary conditions are given by the current continuity equation $\nabla \cdot \boldsymbol{j} = 0$ integrated over the effective thickness of the conducting layer h

$$\boldsymbol{\nabla} \cdot (\Sigma_P \mathbf{E}_\perp) = \pm j_\parallel, \tag{4}$$

and the ionospheric density continuity equation, also integrated in height over h

$$\frac{\partial n_E}{\partial t} = \frac{j_\parallel}{eh} + \alpha\left(n_{E0}^2 - n_E^2\right). \tag{5}$$

Here $\Sigma_P = M_P\, n_E\, h\, e/\cos\psi$; $M_P = 10^4$ m^2/sV (Miura & Sato, 1980) is the ion Pedersen mobility; e is the elementary charge; ψ is the angle between the normal to the ionosphere and the dipole magnetic field at 110 km altitude; and $\alpha = 3 \times 10^{-7}$ cm^3/s (Nygrén et al., 1992) is the coefficient of recombination. In Equation 4, the "+" sign is used in the southern hemisphere and the "−" sign is used in the northern hemisphere. The term αn_E^2 in the right-hand-side of Equation 5 represents losses due to the recombination, and the term αn_{0E}^2 represents the unperturbed source of the ionospheric plasma providing an equilibrium state of the ionosphere, n_{E0}.

The Hall conductivity is not included in Equation 4 because the model is two-dimensional. In general, the Hall conductivity affects the development of the IFI, for example, (Jia & Streltsov, 2014; Pokhotelov et al., 2000), however, its effect can be neglected in the studies focusing on the development of mostly toroidal ULF waves in the magnetospheric resonators with uniform density in the ionosphere. Extensive discussion of the validity of the ionospheric model given by Equations 4 and 5 can be found in Streltsov and Mishin (2018a).

Equations 1–5 are solved numerically by using finite-difference, time-domain (FDTD) technique in the dipole orthogonal coordinate system (L, μ). Here L is the direction perpendicular to the dipole magnetic shell and μ is the direction along the ambient magnetic field. All spatial derivatives are approximated with the second-order finite differences and the temporal dynamics is evaluated with the fourth-order predictor-corrector technique. For the details of the numerical implementation of this algorithm, see, for example, Streltsov and Lotko (1997).

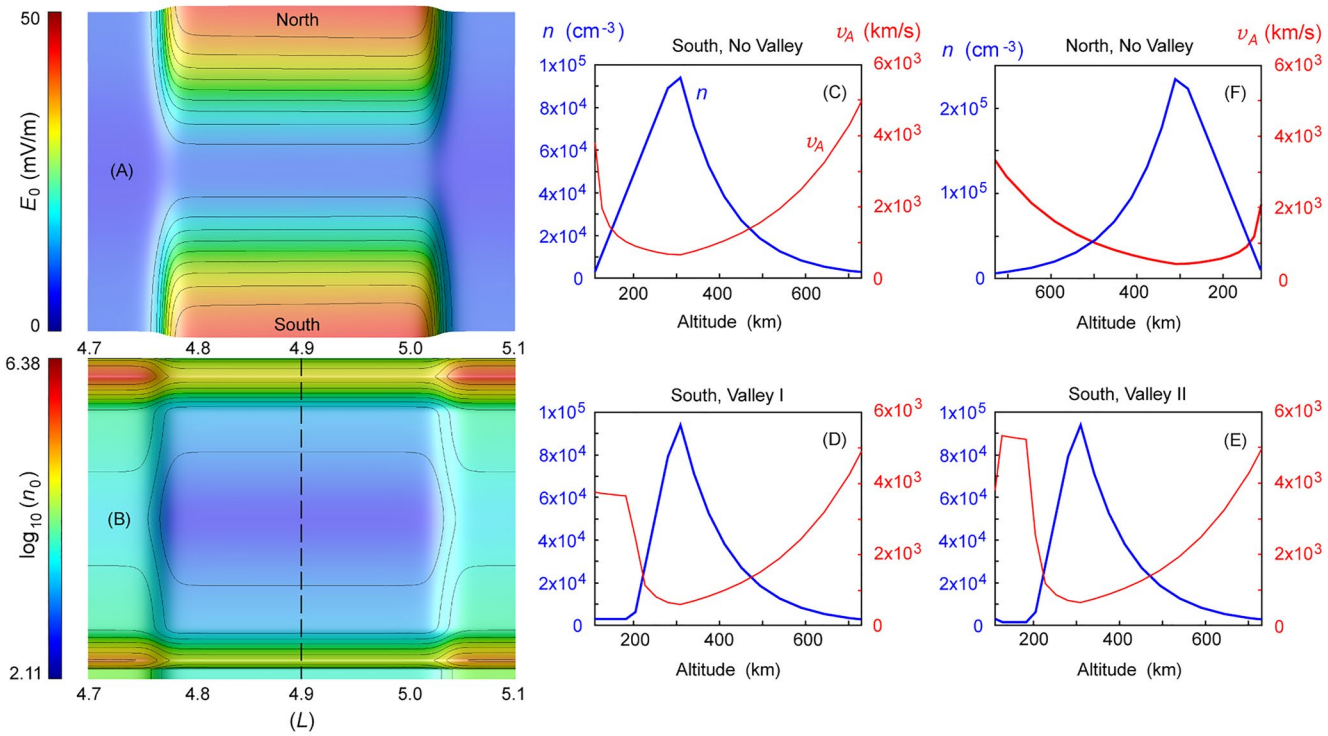

Figure 2. (a) Background perpendicular electric field in the simulation domain. (b) Background plasma density with the ionospheric valley I in the southern hemisphere. Profiles of the plasma density n and the Alfvén velocity v_A at low altitudes in the southern hemisphere: (c) without the ionospheric valley, (d) with the ionospheric valley I, and (e) with the ionospheric valley II. (f) Profiles of n and v_A in the northern hemisphere.

2.1. Background Parameters

The main parameters defining the dynamics, structure, and magnitude of ULF waves and FACs produced by the IFI are the plasma density and the electric field in the ionosphere. We model the development of the IFI driven by the electric field with a maximum amplitude of 50 mV/m in the ionosphere. This is a relatively large-amplitude field which has been observed in the Sub-Auroral Polarization Streams near the plasmapause during substorms, for example, (Mishin et al., 2017; Streltsov & Mishin, 2018b).

The simulation starts from a current-free equilibrium state. This state requires that in the ionosphere, $\nabla \cdot (\Sigma_P \mathbf{E}_\perp) = 0$. This condition means that if the perpendicular electric field is enhanced in some spatial region, then the plasma density should be depleted in the same region.

To satisfy this condition, we specify the density cavity in the ionosphere and find the electric field by solving Equation 4 with the right-hand-side equal to zero. The perpendicular electric field is expressed via the scalar potential ϕ: $\mathbf{E}_\perp = -\nabla\phi$, and this potential is mapped along the ambient magnetic field through the entire domain. The resulting 2D plot of the background $E_\perp$ inside the computational domain is shown in Figure 2a.

The density inside the domain is described with the formula used in several previous studies to reproduce small-scale, intense ULF waves and FACs generated by IFI in good, quantitative details (e.g., Streltsov & Mishin, 2018b, 2020). In a general case, the density in two hemispheres can be different, and the formula for the plasma density without the ionospheric valley is:

$$n_0(L,\mu) = \begin{cases} n1_{N,S}(L)\,(r - r_2) + n2_{N,S}(L), & r_1 < r < r_2 \\ n3_{N,S}(L)\,e^{-(r-r_2)/r_0} + n4_{N,S}(L)/r, & r > r_2 \end{cases} \quad (6)$$

Here, $r = r(L, \mu)$ is the geocentric distance to the point with the dipole coordinates L and μ; $r_0 = 0.0175$; $r_1 = 1 + 110/R_E$ (near the E region maximum); $r_2 = 1 + 300/R_E$ (near the F region maximum); and the functions

$n_{1_{N,S}}(L)$, $n_{2_{N,S}}(L)$, $n_{3_{N,S}}(L)$, and $n_{4_{N,S}}(L)$ define densities in the ionospheric E region, F region, and in the equatorial magnetosphere. In particular, $n_{4_N}(L) \equiv n_{4_S}(L)$ is chosen to provide a density magnitude of 129 cm^{-3} in the equatorial magnetosphere. Functions $n_{2_S}(L)$ is chosen to provide a density magnitude of 1.0×10^5 cm^{-3} in the southern F region, and $n_{2_N}(L)$ is chosen to provide a density of 2.5×10^5 cm^{-3} in the northern F region.

Function $n_{1_S}(L)$ provides a minimum density in the southern E region of 3.0×10^3 cm^{-3}, and $n_{1_N}(L)$ provides a minimum density in the northern E region of 1.0×10^4 cm^{-3}. Plots of the density and the corresponding Alfvén velocity along $L = 4.9$ at the altitudes less than 0.3 R_E are shown in Figure 2c (southern hemisphere) and 2F (northern hemisphere).

The focus of this study is the effect of the ionospheric valley. The valley is implemented in the southern hemisphere (where the density is already lower) by decreasing the density between the altitudes 110 and 200 km. Without valleys the density in the southern hemisphere changes linearly from 3.0×10^3 cm^{-3} at 110 km to 1.0×10^4 cm^{-3} at 300 km altitude. In valley I the density is 3.0×10^3 cm^{-3} between 110 and 200 km altitudes and increases linearly from 3.0×10^3 cm^{-3} to 1.0×10^4 cm^{-3} between 200 and 300 km altitudes. In valley II the density is 3.0×10^3 cm^{-3} at 110 km altitude, it is 1.5×10^3 cm^{-3} between 115 and 200 km, and it increases linearly to 1.0×10^4 cm^{-3} between 200–300 km altitude.

Figure 2b shows 2D plot of the background density with the valley I in the southern hemisphere. Figure 2c shows plots of n and the corresponding v_A along $L = 4.9$ magnetic shell in the altitude range from 110 to 730 km in the southern hemisphere without the ionospheric valleys. Figure 2d shows plots of n and v_A in the southern hemisphere with the ionospheric valley I and Figure 2e shows the same quantities in the case of the ionospheric valley II.

3. Results and Discussion

We ran the simulations of the feedback interactions between ULF Alfvén waves and the ionosphere for 1,600 s. Simulations show that during this time interval, the wave dynamics reach a nonlinear stage and saturates. Figure 3 shows the results from the simulations of the IFI driven by the 50 mV/m electric field when the ionosphere has the valley I in the southern hemisphere. In particular, Figure 3a shows the snapshot of $j_\parallel$ inside the domain taken from the simulations at $t = 512$ s, and Figure 3b shows the snapshot of $j_\parallel$ at $t = 1{,}408$ s Figure 3c shows behavior in time of $j_\parallel$ on $L = 4.9$ at the altitude 110 km in the southern (red line) and northern (blue line) hemispheres. The locations where these values are taken are shown in Figure 3a with red and blue circles correspondingly.

The first conclusion from Figure 3c is that the amplitude of the intensity of FACs generated by the IFI saturates during 1,600 s at the amplitude of ≈30 μA/m^2. These are relatively large currents, but they have been observed on low-orbiting satellites and sounding rockets at high latitudes, for example, (Akbari et al., 2022).

The second conclusion is that the amplitude of negative $j_\parallel$ is larger than the amplitude of positive $j_\parallel$ in the southern hemisphere and vice versa in the northern hemisphere. Also, negative $j_\parallel$ is much narrower than positive $j_\parallel$ in the southern hemisphere and vice versa in the northern hemisphere. Because the negative $j_\parallel$ in the southern hemisphere and positive $j_\parallel$ in the northern hemisphere correspond to the downward FACs, the observed differences in sizes and amplitudes of these currents is explained by the differences in interactions of these currents with the ionosphere. This question has been investigated in the application to the formation of so-called "black" aurora by Streltsov (2018).

The third conclusion is that the magnitude of $j_\parallel$ in the southern hemisphere is less than in the northern hemisphere. This is because the conductivity in the southern hemisphere is less than in the northern hemisphere, and form Equation 4 one can see, that for the same value of $E_\perp$, the lesser Σ_P means lesser $j_\parallel$. This effect has been also discussed by Pokhotelov et al. (2002a) in the application to discrete auroral arcs.

The conclusion from Figure 3c is that the frequency of the large-amplitude non-linear oscillations is two times less than the frequency of the oscillations at the initial stages of the instability. Indeed, the time period of ULF waves near $t = 512$ s is ≈69 s ($f = 14.5$ mHz), and the time period of ULF waves after $t = 1{,}200$ s is ≈145 s ($f = 6.9$ mHz). This effect is explained by the fact that the IFI is always associated with ULF waves standing in the global magnetospheric or local IAR. The structure of the standing waves depends on the boundary conditions, and if these conditions are approximately equal (both are good conductors or insulators), the main power of the resonator is at the fundamental frequency corresponding to the wave with a wavelength equal to two length of the

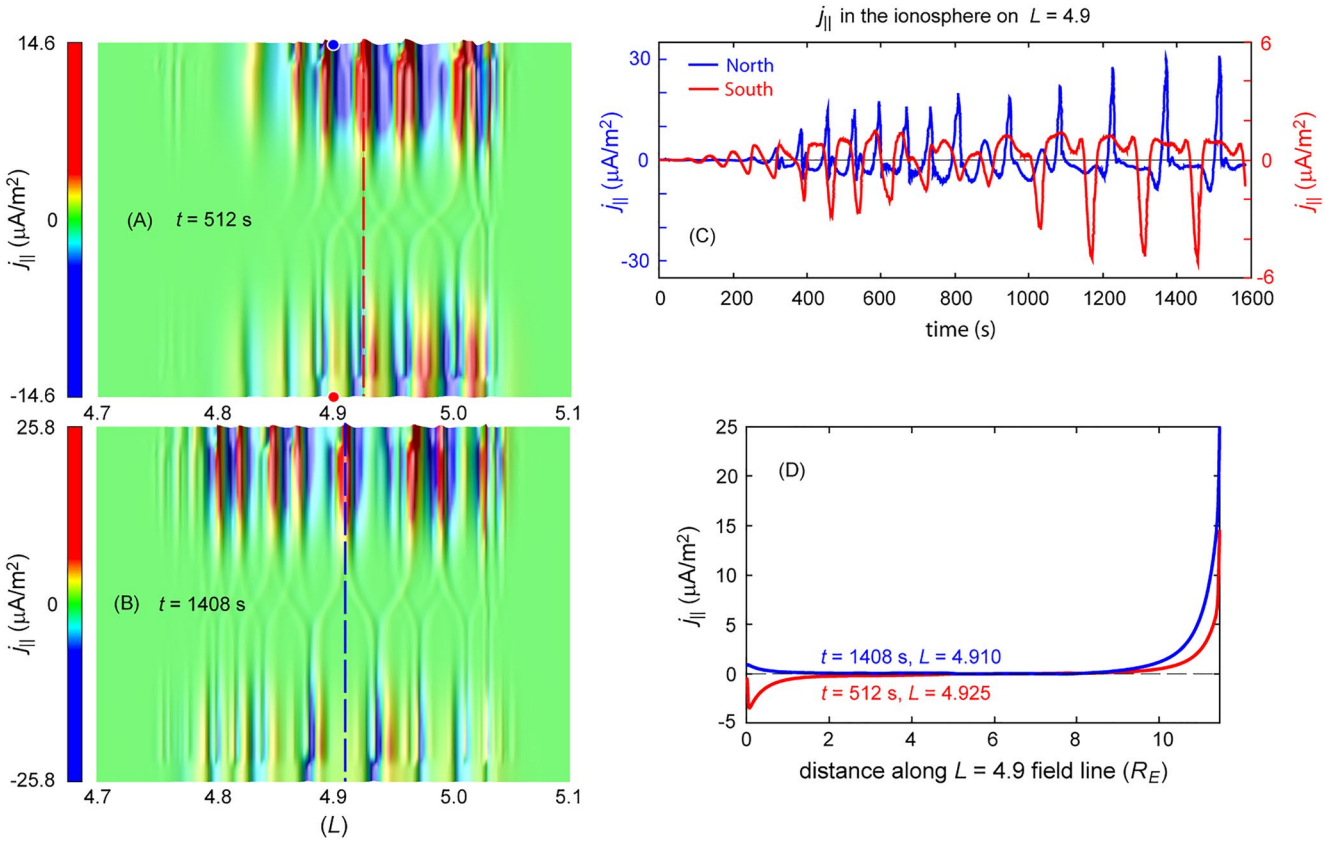

Figure 3. (a) The parallel current density $j_{||}$ in the simulation domain with the ionospheric valley I in the southern hemisphere at t = 512 s; (b) $j_{||}$ at t = 1,408 s. (c) Value of $j_{||}$ on L = 4.9 at 110 km altitude in the northern (blue line) and southern (red line) hemispheres. (d) Profiles of $j_{||}$ at t = 512 s (red) and t = 1,408 s (blue) along the field lines marked with the dashed lines in panels (a) and (b), correspondingly.

resonator. If conditions at two ends of the resonator cavity are very different, then one of them can be considered a conductor and the other an insulator. In this case, the so-called "quarter-waves" may be formed with the frequency equal to half of the fundamental eigenfrequency.

These quarter-waves have been introduced by Allan and Knox (1979a, 1979b) and reported in the observations by Allan (1983); Budnik et al. (1998); Obana et al. (2008, 2015). Lysak et al. (2020) modeled these waves in the global magnetospheric resonator with a non-symmetrical ionospheric conductivity, and Pokhotelov et al. (2000) considered them in the IAR, which walls are formed by the conducting bottom of the ionosphere (conductor) and the gradient in the Alfvén velocity (insulator).

To confirm that the ionospheric feedback mechanism indeed produces quarter-waves, Figure 3d shows $j_{||}$ along ambient magnetic field at t = 512 s (red line) and t = 1,408 s. This $j_{||}$ is taken from the simulations shown in Figures 3a and 3b along the field lines marked with red (L = 4.925) and blue (L = 4.910) dashed lines. On these field lines $j_{||}$ reaches its maximum value at these two moments in time. A comparison of the two profiles shown in Figure 3d demonstrates that, indeed, $j_{||}$ reaches its maximum values in the "half-wavelength" structure at t = 512 s and in the "quarter-wavelength" structure at t = 1,408 s. Although, the maximum values of $j_{||}$ are not reached on the same field line at different moments of time.

Figure 4 illustrates the differences in structure and amplitude of $j_{||}$ produced by the IFI when the ionosphere has no valley (panels a, a', a"), when it has valley I in the southern hemisphere (panels b, b', b"), and when it has valley II in the southern hemisphere (panels c, c', c"). Panels a, b, and c show the dynamics of $j_{||}$ on L = 4.9 at the altitudes 110 km (blue line) and 580 km (red line) in the northern hemisphere, and panels a', b', and c' show them in the southern hemisphere. Panels a", b", and c" show snapshots of $j_{||}$ from the corresponding simulations at t = 1,408 s. Locations in the computational domain where $j_{||}$ is measured to produce plots in panels a, a', b, b', c, c' are marked in Figure 4a" with blue and red circles.

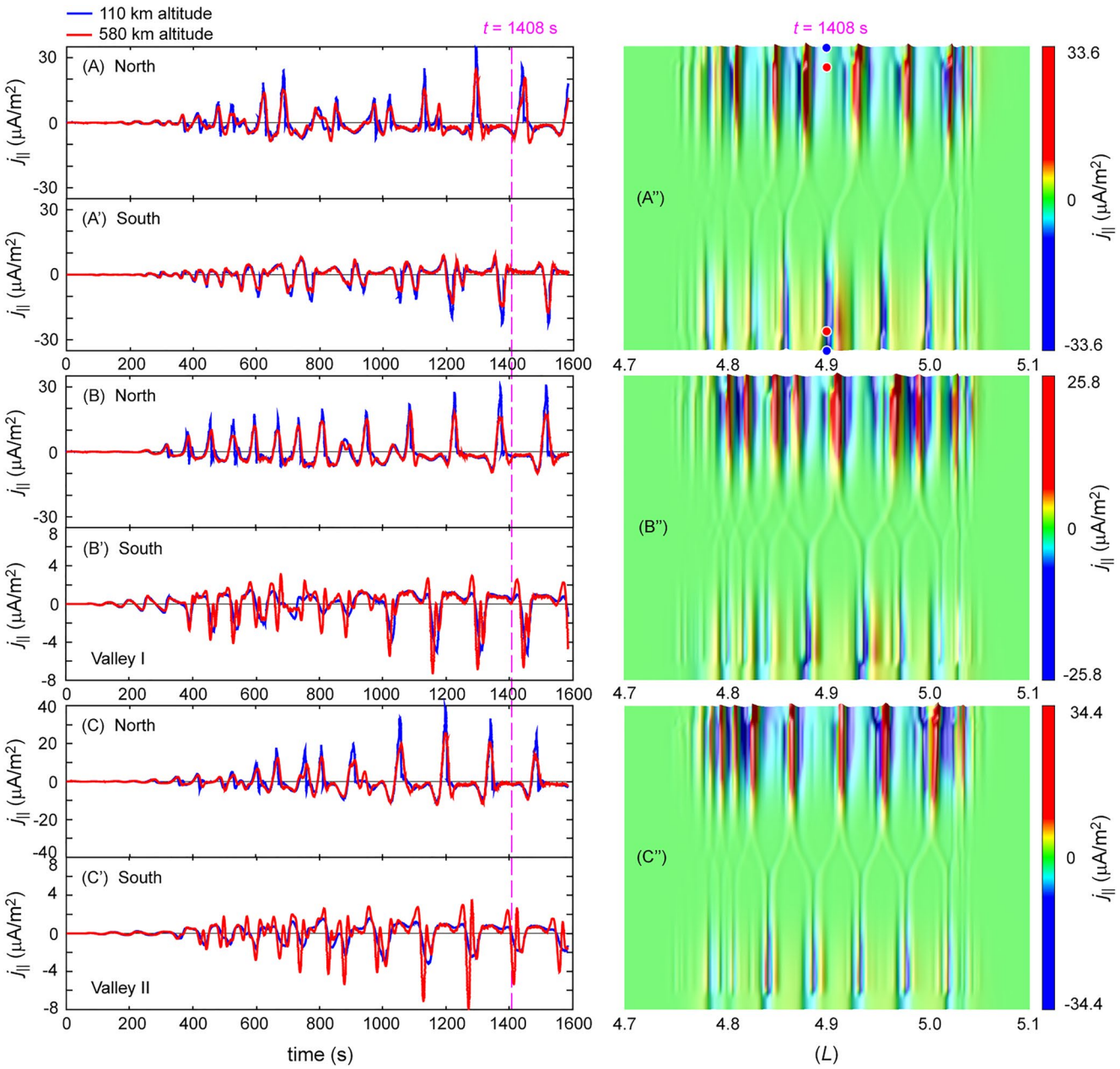

Figure 4. The parallel current density $j_{\parallel}$ on $L = 4.9$ at the altitude 110 km (blue line) and 580 km (red line) in the northern hemisphere in the simulations (a) without the ionospheric valley, (b) with the valley I, and (c) with the valley II. Panels (a'), (b'), and (c') show $j_{\parallel}$ in the southern hemisphere in the corresponding simulations. Panels (a"), (b"), and (c") show snapshots of $j_{\parallel}$ at $t = 1{,}408$ s in the corresponding simulations.

The main conclusion from the results shown in Figure 4 is that the frequency of the large-amplitude waves produced by the IFI in the nonlinear regime in the global resonator with different ionospheric conductivity in two hemispheres is two times less than the frequency of the waves produced by the IFI at the initial stage. In particular, the frequencies of $j_{\parallel}$ shown in Figures 4 and 4a', Figures 4 and 4b', and Figures 4 and 4c' at the time after 1,200 s are 6.8, 6.9, and 7.0 mHz, correspondingly. This means that the strongly non-linear ionospheric feedback produces "quarter-period" standing waves in the global resonator when the ionospheric conductivity in the two hemispheres is different.

Another conclusion from Figure 4b' and 4c' is that when the ionosphere has a valley, then in this hemisphere, the largest amplitude of $j_{\parallel}$ is not at the altitude 110 km (where the ionospheric boundary conditions are implemented) but above it, at ≈580 km. Also, Figure 4c' and 4c" (as well as Figure 4b' and 4b") show that the higher frequency

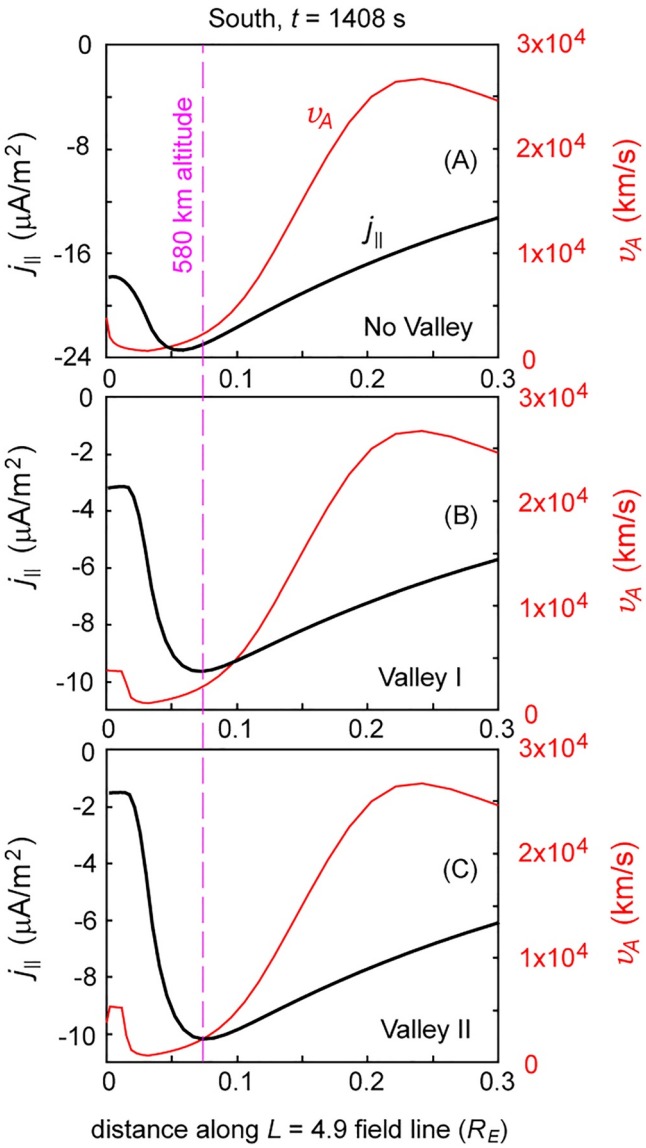

Figure 5. Profiles of $j_{\parallel}$ and v_A at low altitudes in the southern hemisphere from the simulations (a) without the ionospheric valley, (b) with the valley I, and (c) with the valley II at $t = 1{,}408$ s. Each profile is taken along the field line where $|j_{\parallel}|$ reaches maximum value in the southern hemisphere.

structures are developed in the downward currents above the ionospheric valley. The frequencies of these structures are ≈59 mHz in the simulations shown in Figure 4b' (valley I) and ≈35 mHz in the simulations shown in Figure 4c' (valley II).

The parallel structure of $j_{\parallel}$ in the southern hemisphere when the ionosphere there has and does not have valleys is shown in Figure 5. In particular, Figure 5a shows profiles of the background v_A (red line) and $j_{\parallel}$ taken in the southern hemisphere from the simulations without the ionospheric valley at $t = 1{,}408$ s Figure 5b shows v_A and $j_{\parallel}$ from the simulations with the ionospheric valley I, and Figure 5c shows the same quantities from the simulations with the ionospheric valley II. These profiles are taken along the field lines where $j_{\parallel}$ has a minimal value in the southern hemisphere.

The main conclusion derived from Figure 5 is that the amplitude of $j_{\parallel}$ in the southern hemisphere decreases when the ionosphere has a valley. Another conclusion is that the magnitude of $j_{\parallel}$ at 110 km is less than at 580 km when the ionosphere has the valley, and the difference between these magnitudes is larger when the valley is "deeper." These results suggest that the valley lowers the effective ionospheric conductivity by creating a strong gradient in v_A at the upper end of the valley (in our case, at a 200 km altitude). Thus, from the current's point of view, the ionosphere with the valley is "less conductive" than without it, and the reflection of the Alfvén waves from the ionosphere with the low conductivity nullifies the field-aligned current at the reflection point, for example, Mallinckrodt and Carlson (1978); Pokhotelov et al. (2000).

Figure 6 shows plots of $j_{\parallel}$ at the altitudes 110 km (blue lines) and 580 km (red lines) in the northern (A) and southern (B) hemispheres taken from the simulations with the ionospheric valley II at $t = 1{,}408$ s Figure 6b emphasizes the presence of small-scale, higher-frequency (≈35 mHz), FACs in the downward current channels above the ionospheric valley. These currents occur because the ionospheric valley causes a strong gradient in the background v_A at the altitude ≈200 km (see Figures 5b and 5c), which reflects shear ULF Alfvén waves. The reflection coefficient depends on the perpendicular wavelength (Seyler, 1990), and it is larger for the waves with a smaller perpendicular wavelength. Thus, the ionospheric cavity works like a low-pass filter: Waves with larger perpendicular wavelengths propagate through it, and the waves with smaller wavelengths reflect from it.

Now let us consider the development of the IFI when the ionospheric density in both hemispheres is the same. Results from the simulations with a symmetrical density distribution relative to the magnetic equator are shown in Figure 7. Specifically, Figures 7a, 7b, 7c, and 7d show the dynamics of $j_{\parallel}$ on $L = 4.9$ at the altitudes 110 km (blue line) and 580 km (red line) in the northern hemisphere, and Figure 7a', 7b', 7c', and 7d' show them in the southern hemisphere. Figure 7a", 7b", 7c", and 7d" show snapshots of $j_{\parallel}$ from the corresponding simulations at $t = 1{,}408$ s.

Figures 7a and 7a', and 7a" illustrate simulations where the density in both hemispheres is equal to 1.0×10^4 cm^{-3} at the altitude 110 km and 2.5×10^5 cm^{-3} at 300 km. This is the "high Σ_P" case. Figures 7b and 7b', and 7b" illustrate simulations with the density in both hemispheres equal to 0.3×10^4 cm^{-3} at the altitude 110 km and 1.0×10^5 cm^{-3} at 300 km. This is the "low Σ_P" case. Figures 7c and 7c', and 7c" illustrate simulations with the ionospheric valley I in both hemispheres. Figures 7d and 7d', and 7d" illustrate simulations with the ionospheric valley II.

The main conclusion from these simulations is that the ionospheric valley reduces the effective conductivity in the ionosphere, and the decrease of the conductivity in both hemispheres reduces the amplitude of $j_{\parallel}$ generated by

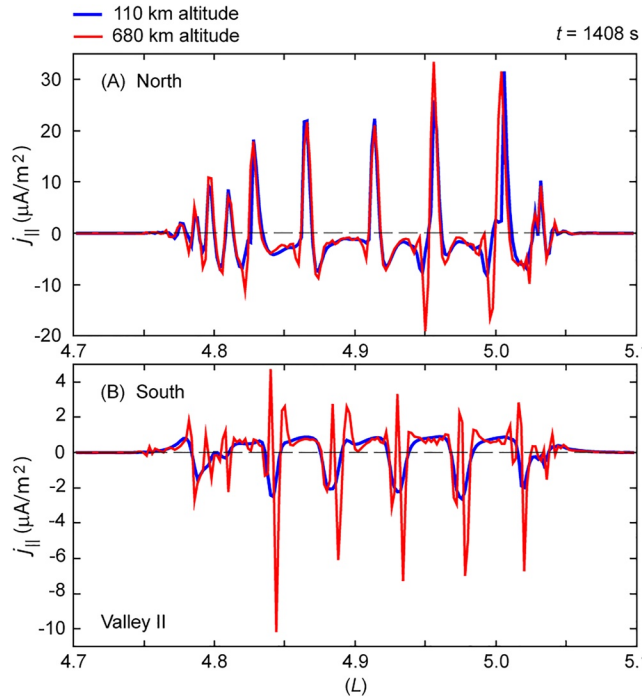

Figure 6. (a) Profiles of $j_{||}$ across the ambient magnetic field at the altitudes 110 km (blue line) and 580 km (red line) in the northern hemisphere in the simulation with the ionospheric valley II at t = 1,408 s. (b) Corresponding profiles of $j_{||}$ in the southern hemisphere.

the instability. Indeed, the amplitude of $j_{||}$ at 110 km altitude in the simulations with the valley I and II (Figures 7c and 7d) is 10 times less than the amplitude of $j_{||}$ in the simulations with the high Σ_P (Figure 7a). Because the amplitude of $j_{||}$ is relatively small in the simulations with the ionospheric valleys, the resonant Alfvén waves keep the half-wavelength, fundamental structure along the ambient magnetic field, and the frequency of the resonant waves does not change with time.

This happens because the field-aligned current changes the ionospheric conductivity in the conjugate hemispheres in the opposite way: it increases the conductivity in one hemisphere and decreases it in another. Thus, due to the active interactions between the field-aligned current and the ionospheric plasma (which is a part of the ionospheric feedback mechanism), the non-symmetrical boundary conditions develop even in the initially symmetrical magnetospheric resonator. The difference between the amplitudes of the ionospheric conductivity in the conjugate hemispheres is proportional to the amplitude of the field-aligned current, and when this difference became large enough (e.g., Lysak et al., 2020) the quartet-period waves have developed.

The frequency of oscillations observed at the altitude 110 km in both hemispheres in the simulations with the ionospheric valleys I is 12.3 mHz, and 11.5 mHz in the simulations with valley II. The frequency of oscillations in the simulations with high Σ_P is 10.5 mHz and it is 11.2 mHz in the simulations with low Σ_P. So the average frequency of ULF waves obtained in the simulations shown in Figure 7 at t = 1,050 s is 11.4 mHz, and all four frequencies obtained in these simulations are within 8% from it.

Figure 8 illustrates the effect of the amplitude of the background electric field on the development of the instability in non-symmetrical hemispheres. In these simulations, the instability is driven by the electric field with the maximum amplitude of 100 mV/m. All other parameters in these simulations (except the maximum amplitude of the electric field) are the same as in the simulations illustrated in Figure 4. Panels a, b, and c show the dynamics of $j_{||}$ on L = 4.9 at the altitudes 110 km (blue line) and 580 km (red line) in the northern hemisphere, and panels a', b', and c' show them in the southern hemisphere. Panels a and a' illustrate the case with non-symmetrical density in different hemispheres and without the ionospheric valley; panels b and b' illustrate the case when the ionosphere in the southern hemisphere has the valley I; panels c and c' illustrate the case when the ionosphere in the southern hemisphere has the valley II.

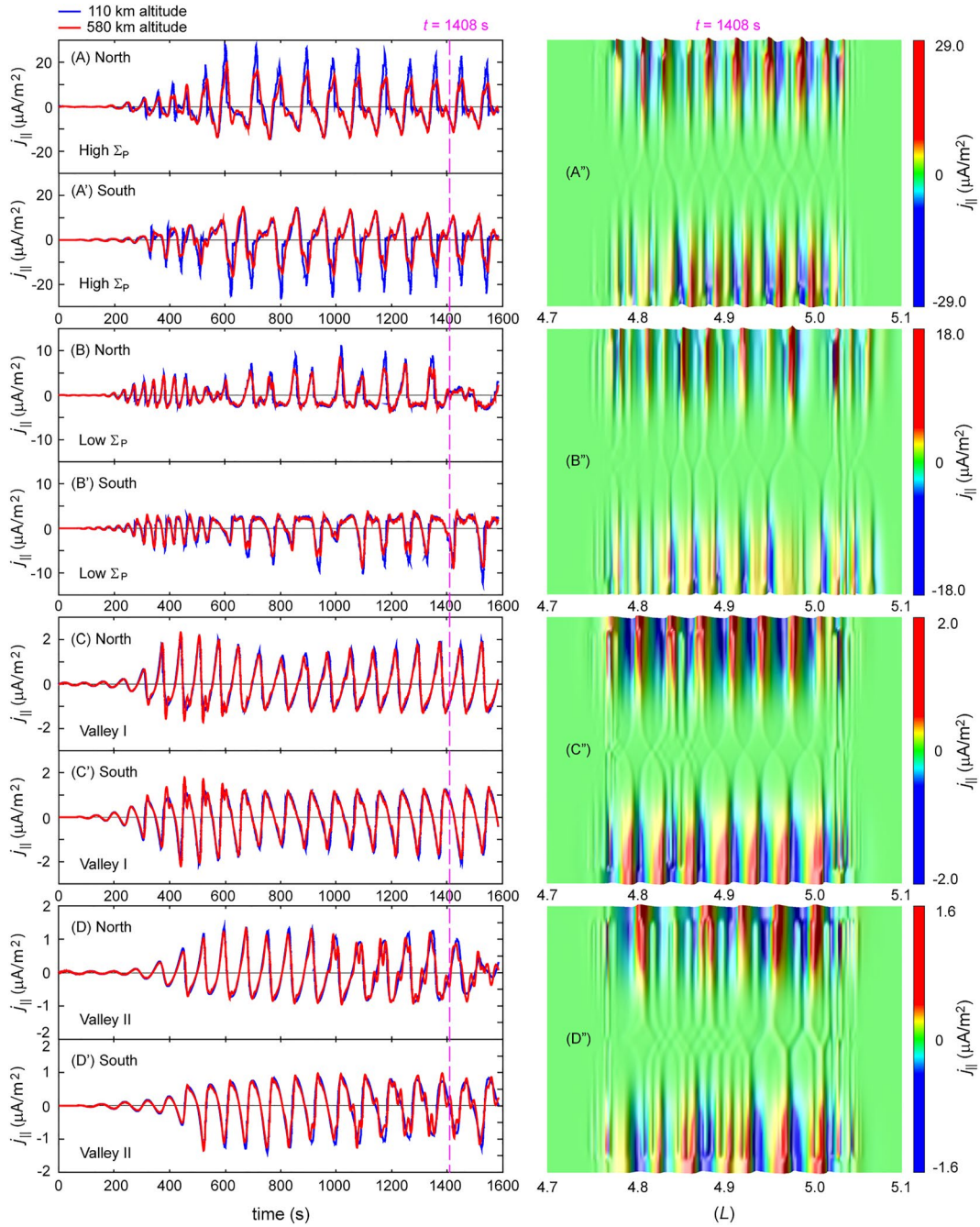

Figure 7. The parallel current density $j_{\parallel}$ on $L = 4.9$ at the altitude 110 km (blue line) and 580 km (red line) in the northern hemisphere in the simulations (a) without the ionospheric valley and high Σ_P in both hemispheres, (b) without the valley and low Σ_P in both hemispheres, (c) with the valley I in both hemispheres, and (d) with the valley II in both hemispheres. Panels (a'), (b'), (c'), and (d') show $j_{\parallel}$ in the southern hemisphere in the corresponding simulations. Panels (a"), (b"), (c"), and (d") show snapshots of $j_{\parallel}$ at $t = 1{,}408$ s in the corresponding simulations.

A comparison between Figures 4 and 8 demonstrates that the amplitude of FACs generated by the IFI driven by the 100 mV/m electric field (Figure 8) is larger than the amplitude of the currents generated by the 50 mV/m field (Figure 4), but other characteristic features of these currents are quite similar. In particular, frequencies of the large-amplitude ULF waves obtained in the simulations illustrated in Figures 8a–8c near 1,200 s are 7.2, 7.1, and 7.7 mHz. These values are close to the values obtained in the simulations with the 50 mV/m large-scale electric field illustrated in Figure 4.

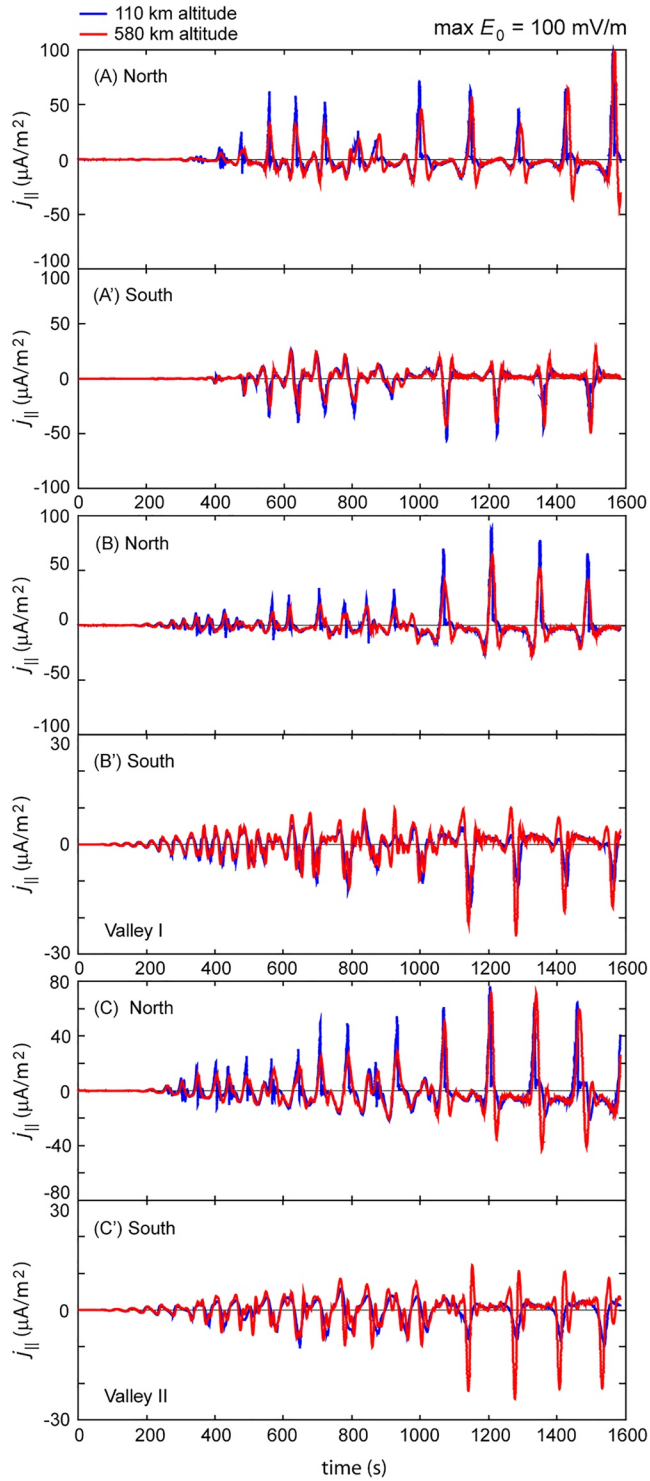

Figure 8. The parallel current density $j_{||}$ on $L = 4.9$ at the altitude 110 km (blue line) and 580 km (red line) in the simulations driven by the 100 mV/m perpendicular electric field. Panels (a), (b), and (c) show $j_{||}$ in the northern hemisphere in the simulations without ionospheric valley, with valley I in the southern hemisphere, and with valley II in the southern hemisphere. Panels (a'), (b'), and (c') show $j_{||}$ in the southern hemisphere in the corresponding simulations.

4. Conclusions

This paper present results from the numerical investigation of intense, small-scale ULF FACs produced by the IFI in the global magnetospheric resonator with strongly non-symmetrical distribution of the plasma density in the conjugate hemispheres. The asymmetry in density has been enhanced by the introduction of the ionospheric valley in the hemisphere where the plasma density is already lower. The results from this study are as follows:

- Simulations show that in both hemispheres, the amplitude of the downward currents produced by the instability in its nonlinear stage is larger than the amplitude of the upward currents, and the transverse size of the downward currents is much smaller than the size of the upward currents.
- Simulations also show that the frequency of the large-amplitude waves produced by the IFI in the nonlinear regime in the global resonator with different ionospheric conductivity in two hemispheres is two times less than the frequency of the waves produced by the IFI at the initial stage. This means that the strongly non-linear ionospheric feedback produces "quarter-period" standing waves in the non-symmetrical global magnetospheric resonator.
- The ionospheric valley decreases the effective conductivity of the ionosphere. It makes the ionosphere "less conductive" from the field-aligned current point of view, and decreases the magnitude of the current above that ionosphere.
- Also, the ionospheric valley creates a strong gradient in v_A at the upper end of the valley which reflects ULF Alfvén waves. The reflection from the density gradient depends on the perpendicular wavelength: the waves with smaller perpendicular wavelength reflect stronger than the larger-wavelength waves. Thus, the ionospheric cavity works like a low-pass filter: Waves with larger perpendicular wavelengths propagate through it, and the waves with smaller wavelengths reflect from it. As a result, the perpendicular structure of the ULF waves and FACs is different at different altitudes.

Data Availability Statement

The codes used in the simulations, the data files used to run the codes, and the results from the simulation shown in Figures 3, 4, 7 and 8 are available from https://figshare.com (https://doi.org/10.6084/m9.figshare.19768750).

Acknowledgments
E. V. Mishin acknowledges support by the Air Force Office of Scientific Research LRIR 22RVCOR011, and A. V. Streltsov acknowledges support by the NSF award AGS 1803702. Approved for public release; distribution is unlimited. Public Affairs release approval # AFRL-2022-2641. The views expressed are those of the authors and do not reflect the original guidance or position of the United State Government, the Department of Defense, or the United States Air Force. The appearance of external hyperlinks does not constitute endorsement by the United States Department of Defense (DoD) of the linked websites, or the information, products, or services contained therein. The DoD does not exercise any editorial, security, or other control over the information you may find at these locations.

References

Akbari, H., Pfaff, R., Clemmons, J., Freudenreich, H., Rowland, D., & Streltsov, A. (2022). Resonant Alfvén waves in the lower auroral ionosphere: Evidence for the nonlinear evolution of the ionospheric feedback instability. *Journal of Geophysical Research: Space Physics*, *127*(2), e2021JA029. https://doi.org/10.1029/2021JA029854

Allan, W. (1983). Quarter-wave ULF pulsations. *Planetary and Space Science*, *31*(3), 323–330. https://doi.org/10.1016/0032-0633(83)90083-1

Allan, W., & Knox, F. (1979a). A dipole field model for axisymmetric Alfvén waves with finite ionosphere conductivities. *Planetary and Space Science*, *27*(1), 79–85. https://doi.org/10.1016/0032-0633(79)90149-1

Allan, W., & Knox, F. (1979b). The effect of finite ionosphere conductivities on axisymmetric toroidal Alfvén wave resonances. *Planetary and Space Science*, *27*(7), 939–950. https://doi.org/10.1016/0032-0633(79)90024-2

Atkinson, G. (1970). Auroral arcs: Result of the interaction of a dynamic magnetosphere with the ionosphere. *Journal of Geophysical Research*, *75*(25), 4746–4755. https://doi.org/10.1029/ja075i025p04746

Budnik, F., Stellmacher, M., Glassmeier, K., & Buchert, S. C. (1998). Ionospheric conductance distribution and MHD wave structure: Observation and model. *Annales Geophysicae*, *16*(2), 140–147. https://doi.org/10.1007/s00585-998-0140-8

Chmyrev, V. M., Bilichenko, S. V., Pokhotelov, O. A., Marchenko, V. A., Lazarev, V. I., Streltsov, A. V., & Steflo, L. (1988). Alfvén vortices and related phenomena in the ionosphere and the magnetosphere. *Physica Scripta, 38*(6), 841–854. https://doi.org/10.1088/0031-8949/38/6/016

Goertz, C., & Boswell, R. (1979). Magnetosphere-ionosphere coupling. *Journal of Geophysical Research*, *84*(A12), 7239. https://doi.org/10.1029/ja084ia12p07239

Hasegawa, A. (1976). Particle acceleration by MHD surface wave and formation of aurora. *Journal of Geophysical Research*, *81*(28), 5083–5090. https://doi.org/10.1029/ja081i028p05083

Jia, N., & Streltsov, A. (2014). Ionospheric feedback instability and active discrete auroral forms. *Journal of Geophysical Research*, *119*(3), 2243–2254. https://doi.org/10.1002/2013JA019217

Kelley, M. C. (1989). *The Earth's ionosphere*. Elsevier, Academic Press.

Lysak, R. L. (1991). Feedback instability of the ionospheric resonant cavity. *Journal of Geophysical Research*, *96*(A2), 1553–1568. https://doi.org/10.1029/90ja02154

Lysak, R. L., Song, Y., Waters, C. L., Sciffer, M. D., & Obana, Y. (2020). Numerical investigations of interhemispheric asymmetry due to ionospheric conductance. *Journal of Geophysical Research*, *125*(7), e2020JA027. https://doi.org/10.1029/2020JA027866

Mallinckrodt, A. J., & Carlson, C. W. (1978). Relations between transverse electric fields and field-aligned currents. *Journal of Geophysical Research*, *83*(A4), 1426. https://doi.org/10.1029/ja083ia04p01426

Mishin, E. V., Nishimura, Y., & Foster, J. (2017). SAPS/SAID revisited: A causal relation to the substorm current wedge. *Journal of Geophysical Research*, *122*(8), 8516–8535. https://doi.org/10.1002/2017JA024263

Miura, A., & Sato, T. (1980). Numerical simulation of global formation of auroral arcs. *Journal of Geophysical Research*, *85*(A1), 73–91. https://doi.org/10.1029/ja085ia01p00073

Nygrén, T., Kaila, K., Huuskonen, A., & Turunen, T. (1992). Determination of E region effective recombination coefficient using impulsive precipitation events. *Geophysical Research Letters*, *19*(5), 445–448. https://doi.org/10.1029/92gl00118

Obana, Y., Menk, F. W., Sciffer, M. D., & Waters, C. L. (2008). Quarter-wave modes of standing Alfvén waves detected by cross-phase analysis. *Journal of Geophysical Research*, *113*(A8), A08203. https://doi.org/10.1029/2007JA012917

Obana, Y., Waters, C. L., Sciffer, M. D., Menk, F. W., Lysak, R. L., Shiokawa, K., et al. (2015). Resonance structure and mode transition of quarter-wave ULF pulsations around the dawn terminator. *Journal of Geophysical Research*, *120*(6), 4194–4212. https://doi.org/10.1002/2015JA021096

Pokhotelov, D., Lotko, W., & Streltsov, A. V. (2002a). Effects of the seasonal asymmetry in ionospheric Pedersen conductance on the appearance of discrete aurora. *Geophysical Research Letters*, *29*(10), 79-1–79-4. https://doi.org/10.1029/2001GL014010

Pokhotelov, D., Lotko, W., & Streltsov, A. V. (2002b). Harmonic structure of field-line eigenmodes generated by ionospheric feedback instability. *Journal of Geophysical Research*, *107*(A11), 1363. https://doi.org/10.1029/2001JA000134

Pokhotelov, D., Lotko, W., & Streltsov, A. V. (2004). Simulations of resonant alfvén waves generated by artificial HF heating of the auroral ionosphere. *Annales Geophysicae*, *22*(8), 2943–2949. https://doi.org/10.5194/angeo-22-2943-2004

Pokhotelov, O., Pokhotelov, D., Streltsov, A., Khruschev, V., & Parrot, M. (2000). Dispersive ionospheric Alfvén resonator. *Journal of Geophysical Research*, *105*(A4), 7737–7746. https://doi.org/10.1029/1999ja900480

Robinson, T. R., Strangeway, R., Wright, D. M., Davies, J. A., Horne, R. B., Yeoman, T. K., et al. (2000). FAST observations of ULF waves injected into the magnetosphere by of modulated RF heating of the auroral electrojet. *Geophysical Research Letters*, *27*(19), 3165–3168. https://doi.org/10.1029/2000gl011882

Sato, T. (1978). A theory of quiet auroral arcs. *Journal of Geophysical Research*, *83*(A3), 1042. https://doi.org/10.1029/ja083ia03p01042

Seyler, C. (1990). A mathematical model of the structure and evolution of small-scal discrete auroral arcs. *Journal of Geophysical Research*, *95*(10), 17199. https://doi.org/10.1029/ja095ia10p17199

Streltsov, A. (2018). On the asymmetry between upward and downward field-aligned currents interacting with the ionosphere. *Journal of Geophysical Research*, *123*(11), 9275–9285. https://doi.org/10.1029/2018JA025826

Streltsov, A., Berthelier, J.-J., Chernyshov, A., Frolov, V., Honary, F., Kosch, M., et al. (2018). Past, present and future of active radio frequency experiments in space. *Space Science Reviews*, *214*(8), 118. https://doi.org/10.1007/s11214-018-0549-7

Streltsov, A., & Lotko, W. (1997). Dispersive, nonradiative field line resonances in a dipolar magnetic field geometry. *Journal of Geophysical Research*, *102*(A12), 27121–27135. https://doi.org/10.1029/97JA02530

Streltsov, A., & Lotko, W. (2004). Multiscale electrodynamics of the ionosphere-magnetosphere system. *Journal of Geophysical Research*, *109*(A9), 457. https://doi.org/10.1029/2004JA010

Streltsov, A., & Mishin, E. (2018a). On the existence of ionospheric feedback instability in the earth's magnetosphere-ionosphere system. *Journal of Geophysical Research*, *123*(11), 8951–8957. https://doi.org/10.1029/2018JA025942

Streltsov, A., & Mishin, E. (2018b). Ultralow frequency electrodynamics of magnetosphere-ionosphere interactions near the plasmapause during substorms. *Journal of Geophysical Research*, *123*(9), 7441–7451. https://doi.org/10.1029/2018JA025899

Streltsov, A., & Mishin, E. (2020). ULF waves generated near the plasmapause by the magnetosphere-ionosphere interactions. *Journal of Geophysical Research: Space Physics*, *125*(2), e2019JA027. https://doi.org/10.1029/2019JA027353

Titheridge, J. (2003). Ionization below the night F2 layer—A global model. *Journal of Atmospheric and Solar-Terrestrial Physics*, *65*(9), 1035–1052. https://doi.org/10.1016/S1364-6826(03)00136-6

Trakhtengertz, V., & Feldstein, A. (1981). Influence of Alfvén velocity inhomogeneous profile on magnetospheric convection stratification. *Geomagnetism and Aeronomy*, *21*, 951.

Trakhtengertz, V., & Feldstein, A. (1991). Turbulent Alfvén boundary layer in the polar ionosphere. 1. Excitation conditions and energetics. *Journal of Geophysical Research*, *96*(A11), 19363. https://doi.org/10.1029/91ja00376

Watanabe, T., Oya, H., Watanabe, K., & Sato, T. (1993). Comprehensive simulation study on local and global development of auroral arcs and field-aligned potentials. *Journal of Geophysical Research*, *98*(A12), 21391–21407. https://doi.org/10.1029/93ja01769